

Solvent-mediated partial ionicity enhances mechanical nanosizing effect of Mg-based hydrogen storage alloys

Received: 22 May 2025

Accepted: 5 January 2026

Published online: 14 January 2026

 Check for updatesTianpeng Sun^{1,2,3,4}, Zhengjie Tang⁵, Jiang Liu^{1,2,3,4}, Xuan Sun⁶, Qun Luo⁶, Yu Zhang¹, Qian Li^{1,2,3,4,5} & Yangfan Lu^{1,2,3,4,5} ✉

The high ductility of Mg has posed major challenges for nanofabrication utilizing mechanical ball-milling. While the addition of organic solvents is effective, it has been unclear how they improve the ball-milling effect by modifying the material's surface properties. Herein, we report that the solvent-mediated partial ionicity plays an important role in enhancing the nanosizing effect of Mg_{87.5}Ni_{5.5}Y₇ alloy. This approach enables the Mg_{87.5}Ni_{5.5}Y₇ particles to be 88 times smaller than those of the solvent-free procedure. The Mg_{87.5}Ni_{5.5}Y₇ nanoparticles underwent complete dehydrogenation in 3 min at 300 °C and in 17 min at 240 °C, which can be stably cycled at least for 500 times. Solvent (THF) adsorption on Mg induces Mg^{δ+}–Mg^{δ-} dipole structure. This increases the surface hardness of Mg-based alloy and maximizes the ball milling-driven structural deformation, thereby facilitating ion migration. Mg–Mg bond breaking is caused by the resulting Coulombic repulsion between Mg atoms. These findings provide an affordable approach for nanoparticle fabrication of highly ductile materials.

Hydrogen, as a zero-carbon energy carrier, exhibits impressive characteristics of abundance, versatile application, and high energy conversion efficiency. Unfortunately, its widespread application is constrained by critical challenges in hydrogen storage and transportation sectors¹. Magnesium (Mg) has emerged as a promising candidate, given its prominent theoretical hydrogen storage capacity (7.6 wt.% H₂), environmental friendliness and abundant natural reserves^{2–10}. Despite these advantages, Mg faces limitations due to its sluggish reaction kinetics, which stem from multistep reaction processes, including hydrogen adsorption, dissociation, diffusion and nucleation. These processes necessitate high operation temperature (~350 °C) and substantial energy loss^{11,12}.

To enhance the kinetic processes, a variety of Mg-based alloys, such as Mg–Ni–RE (RE = rare earths), have been developed^{13–16}. They

undergo in situ decomposition after the activation process and generate Mg, Mg₂Ni, and REH_x nanoparticles (NPs). In it, Mg contributes hydrogen storage capacity, while REH_x and Mg₂Ni serve as catalyst phases for hydrogen adsorption and dissociation, thereby enhancing the rates of hydrogenation and dehydrogenation (de/hydrogenation)^{17–21}. However, the hydrogen diffusion in the Mg phase is hardly accelerated by these catalyst phases, and persistent challenges of coarse particle size distribution and suboptimal morphology control are still unresolved^{22,23}.

Nanostructuring strategies demonstrate transformative potential^{24,25}. Nanoparticles increase their surface energies thanks to the unsaturated coordination number, increased grain boundaries and enriched reaction sites/defects, which accelerate hydrogen adsorption and dissociation^{26–28}. Furthermore, nanoscale dimensions shorten

¹College of Materials Science and Engineering, Chongqing University, Chongqing, China. ²National Engineering Research Center for Magnesium Alloy, Chongqing University, Chongqing, China. ³National Key Laboratory of Advanced Casting Technologies, Chongqing University, Chongqing, China. ⁴National Innovation Center for Industry-Education Integration of Energy Storage Technology, Chongqing University, Chongqing, China. ⁵Chongqing Institute of New Energy Storage Materials and Equipment, Chongqing, China. ⁶School of Materials Science and Engineering, Shanghai University, Shanghai, China.

✉ e-mail: yangfanlu@cqu.edu.cn

hydrogen diffusion paths between surface and bulk regions, significantly ramping de/hydrogenation rates²⁹. Combining Ni catalysts with nanostructured Mg simultaneously accelerates hydrogen adsorption, dissociation, diffusion and nucleation. Nanofabrication of Mg can drastically enhance de/hydrogenation rates at much milder reaction temperatures^{4,5,8,29–32}. Room-temperature reversible hydrogen storage of Mg can even be achieved at particle sizes below ~5 nm³³. While the current nanofabrication method can improve scalability, it predominantly relies on gas atomization and chemical reduction processes, which requires expensive precursors and complicated synthetic procedures, posing major challenges for industry utilization.

In contrast, mechanical ball milling offers a simpler and cost-effective alternative, and a variety of ball-milling studies on both Mg-based compounds, such as MgH₂, have been reported^{34–39}. However, unlike the brittle ceramic MgH₂, the high ductility of metallic Mg fundamentally hinders its applicability due to severe agglomeration and cold welding^{40,41}. Recent advances in solvent-assisted ball milling show promise. Zou et al.⁴² successfully synthesized nanoscale Mg via this approach, providing a scalable route for the nanoparticle production of Mg. However, the mechanistic role of solvents in enabling Mg nanosizing is still unclear. In addition, surface instability after ball-milling poses challenges for practical applications. These issues collectively impede the development of milder-temperature operable Mg-based hydrogen storage materials.

Herein, we report that the partial ionicity induced by solvent adsorption on Mg-based alloy (Mg_{87.5}Ni_{5.5}Y₇) can improve nanosizing effects during ball-milling. The solvent-assisted process yielded particles as small as ~511.87 nm, representing an 88-fold size reduction compared to solvent-free milling (~44.89 μm). The nanostructured Mg_{87.5}Ni_{5.5}Y₇ exhibited dehydrogenation rates of 1.71 wt.% min⁻¹ at 300 °C and 0.46 wt.% min⁻¹ at 240 °C, surpassing the previously reported related Mg-based alloys. Density functional theory (DFT) calculations revealed that solvent (THF) adsorption on Mg surfaces induces electron redistribution. Mg atoms bonded to oxygen lose 0.56 e⁻, while adjacent Mg atoms gain partial electrons. It gives rise to partial ionicity in Mg (Mg^{δ+}–Mg^{δ-} dipole structure), and as a result, the surface hardness (Vickers hardness) is ~22% enhanced by THF-adsorption. The ion migration during balling induces Coulombic repulsion between Mg atoms, maximizing stress-driven structural deformation and subsequent nanoparticle formation. The present data demonstrates the microscopic role of solvents on modifying the material's surface electronic structure and mechanical properties, offering an affordable strategy for nanoparticle fabrication.

Results and discussion

Solvent-Assisted Ball-Milling of Mg_{87.5}Ni_{5.5}Y₇

Figure 1a illustrates the powdering process achieved through mechanical impact, such as ball milling, of metallic and ionic compounds. Metallic materials are characterized by delocalized electrons, and structural deformation contributes a little to the metallic bond structure, resulting in more ductile properties. Meanwhile, ionic materials involve both positively and negatively charged ions. The slight modification of crystal deformation immediately gives rise to Coulombic repulsion between identically charged ions and generates cracks. Therefore, it is widely believed that ionic materials are more susceptible to mechanical impact and are easily nanosized by ball-milling. Mg_{87.5}Ni_{5.5}Y₇ is one of the Mg-based alloys that is characterized by highly ductile properties. Prior to THF adsorption, ball-milling does not provide a powdering effect to the Mg_{87.5}Ni_{5.5}Y₇ alloy, and the mean particle size was estimated to be 44.89 μm (Fig. 1b and Supplementary Figs. S1 and S2). Meanwhile, introducing 1 mL THF significantly enhanced the ball-milling effect. The THF-assisted milling achieved a mean particle size of 511.87 nm, an 88-fold reduction compared to the solvent-free process. Its BET area was measured as 3.72 m²·g⁻¹ (Fig. 1c). The particle size distribution analysis indicates that 78 % of the

particulates fall within the range of 300–900 nm, highlighting the efficacy of THF-assisted milling in achieving uniform dispersion and considerable nanosizing during the ball-milling process.

High-resolution TEM (HRTEM) characterization of the Mg_{87.5}Ni_{5.5}Y₇ alloy (Fig. 1d) reveals characteristic lattice fringes with measured d-spacings of 0.19 nm, which corresponds to the (102) plane of hexagonal close-packed Mg. It agrees well with the XRD data, in which Mg and Mg₂Ni were observed as major and minor phases, respectively (Supplementary Fig. S3). EDS elemental mapping verifies homogeneous distribution of Mg and Y across the matrix, whereas Ni demonstrates preferential segregation within the Mg₂Ni domains. These findings are further supported by XPS analysis of the electronic states of the elements within Mg_{87.5}Ni_{5.5}Y₇ NPs. Specifically, Mg displays a Mg⁰ peak at 1303.5 eV, metallic Ni 2p_{3/2} signatures at 852.7 eV in Mg₂Ni phases, and the Y 3d spectrum reveals spin-orbit resolved doublets where the 3d_{5/2} component at 156.8 eV is assigned to Y⁶⁺ (Fig. 1e–g). These XPS characteristics are consistent with Mg–Ni–Y alloys reported elsewhere^{43,44}, demonstrating that the Mg_{87.5}Ni_{5.5}Y₇ NPs are not oxidized during the nanosizing process.

It is emphasized that not all solvents can enhance the nanosizing effect of ball-milling. As shown in Supplementary Fig. S4, the addition of cyclohexane exhibits little contribution to ball-milling efficiency, and the observed mean particle size is largely consistent with that of the dry-milled samples. The mechanism difference of THF- and cyclohexane-assisted nanosizing effect will be discussed later.

Hydrolysis corrosion properties

While nanosizing enhances the hydrogen storage capability of Mg-based hydrogen storage materials, it also increases their surface areas, thereby worsening the material's chemical stability. This is because the increased surface area provides more reactive sites for impurities such as water to form Mg(OH)₂. The degradation of Mg₂Ni further exacerbates the surface corrosion rates⁴⁵. To tackle the contradiction between hydrogen storage performance and chemical stability of Mg_{87.5}Ni_{5.5}Y₇ NPs, we applied PMMA coatings. In this study, we synthesized Mg_{87.5}Ni_{5.5}Y₇ NPs with 0, 0.1, 0.5, and 1.0 wt.% PMMA content and successfully suppressed the surface corrosion rates (Fig. 2a). Uncoated nanoparticles exhibited severe hydrogen corrosion with a rapid hydrogen evolution at 51.0 mL·g⁻¹·min⁻¹ during the first 3 minutes (Fig. 2b). Meanwhile, the H₂ production rate of Mg_{87.5}Ni_{5.5}Y₇ NPs with 0.1, 0.5, and 1.0 wt.% PMMA content were estimated to be 14.7 mL·g⁻¹·min⁻¹, 7.0 mL·g⁻¹·min⁻¹ and 5.6 mL·g⁻¹·min⁻¹, respectively, representing a 71.2–89.0 % reduction compared to the PMMA-free system (Fig. 2b and Supplementary Figs. S5 and S6). The suppression of H₂ evolution is interpreted by the polymer's (e.g., PMMA) protection effect that suppress direct contact between Mg_{87.5}Ni_{5.5}Y₇ NPs and water, which is consistent with previous studies^{4,22,46–49}.

Figure 2c shows the XRD pattern of water-exposed uncoated and 0.1 wt.% PMMA coated Mg_{87.5}Ni_{5.5}Y₇ NPs. While the uncoated samples exhibit major Mg(OH)₂ peaks, the corresponding peaks are much suppressed for the 0.1 wt.% PMMA-coated samples. To further confirm the surface protection effect of PMMA, we exposed the uncoated and 0.1 wt.% PMMA-coated Mg_{87.5}Ni_{5.5}Y₇ NPs under an ambient atmosphere for two weeks (Fig. 2d). Again, a notable Mg(OH)₂ peak was confirmed for the uncoated samples, due to the reaction with air moisture. Meanwhile, the XRD is largely unchanged for 0.1 wt.% PMMA-coated Mg_{87.5}Ni_{5.5}Y₇ NPs, and both Mg(OH)₂ and MgO peaks were not identified. These data demonstrated improved surface stability by the PMMA coating.

Hydrogen storage performances

To investigate the effects of nanosizing and surface modification on the dehydrogenation kinetics of Mg_{87.5}Ni_{5.5}Y₇, we conducted dehydrogenation experiments on samples with and without PMMA coating. Prior to the kinetics analysis, all of the samples were activated utilizing

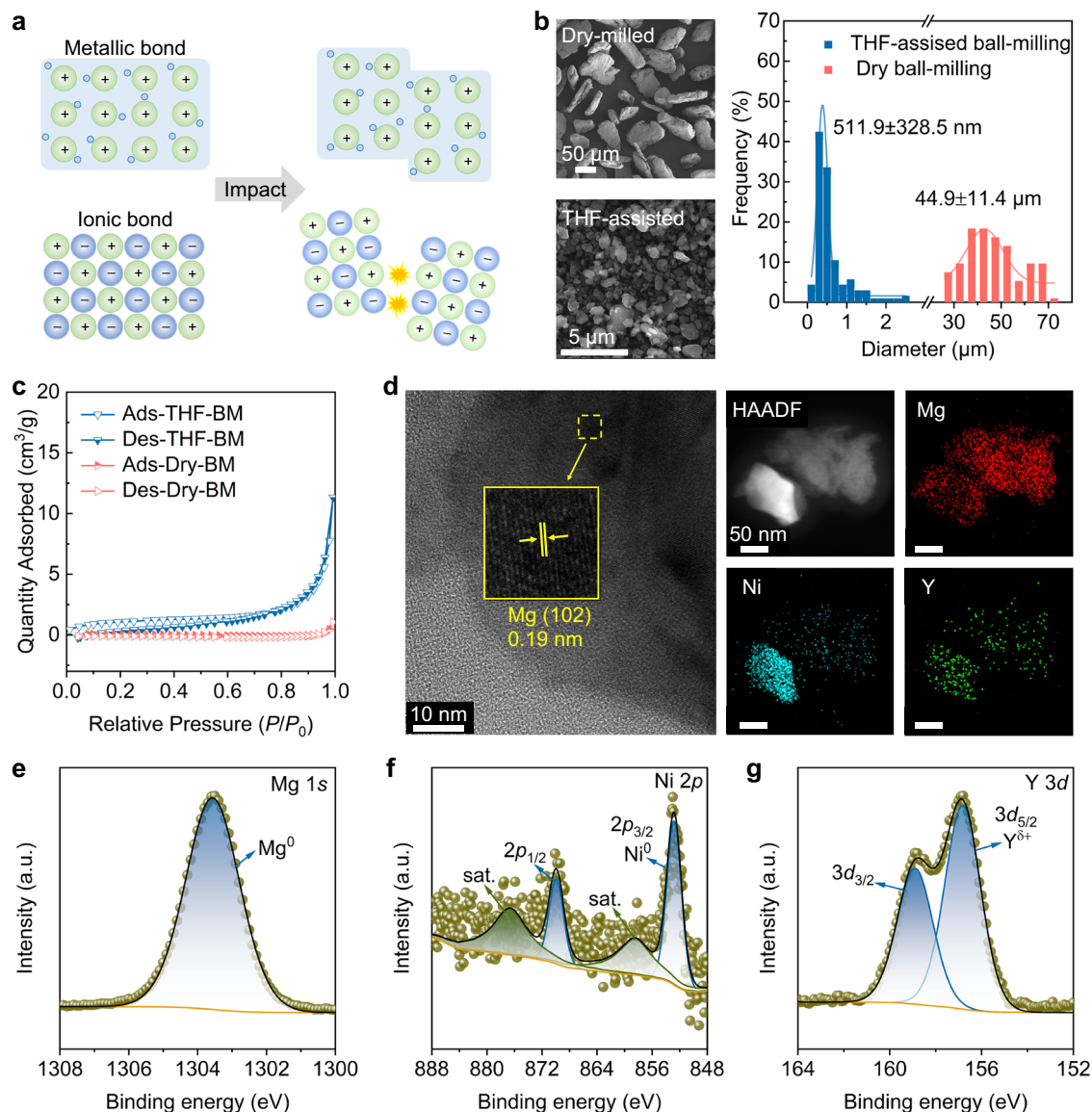


Fig. 1 | Morphology and chemical properties of Mg_{87.5}Ni_{5.5}Y₇ NPs. **a** Schematic illustration of mechanical impact to the metallic and ionic compounds. The light blue region represents the distributed free electrons. **b** SEM image and mean particle size distribution of dry and THF-assisted ball-milled Mg_{87.5}Ni_{5.5}Y₇ alloy. The solid lines represent a Gaussian fit. The error bars were given utilizing the standard deviation of 147 particle data. **c** Adsorption isotherm of dry and THF-assisted ball-milled Mg_{87.5}Ni_{5.5}Y₇ alloy. **d** HRTEM images and corresponding EDS mapping of

THF-assisted ball-milled Mg_{87.5}Ni_{5.5}Y₇ alloy. The inset represents the (102) lattice plane of Mg. The red, light-blue and green dots represent Mg, Ni and Y elements, respectively. **e–g** XPS spectra of Mg_{87.5}Ni_{5.5}Y₇ NPs. The dots and solid lines represent experimental data and fitting results. During the fitting of the Mg 1s, Ni 2p, and Y 3d core-level spectra, the full width at half maximum (FWHM) was constrained to be identical for multiple peaks belonging to the same chemical state. Their area ratios (shaded region) were also fixed with the theoretical ratio.

de/hydrogenation cycles. While Mg_{87.5}Ni_{5.5}Y₇ NPs (THF-assisted ball-milled samples) are easily activated, the dry-milled samples cannot be activated under the same conditions (Supplementary Fig. S7). After the activation, the Mg_{87.5}Ni_{5.5}Y₇ NPs transform to MgH₂-Mg₂Ni-YH₃ nanocomposite, whose BET surface area is 9.51 m²·g⁻¹ (Supplementary Fig. S8). In it, both Mg₂Ni and YH₃ exhibit improved hydrogen adoption and dissociation capability, which serve as catalytically active phases (Supplementary Fig. S9). In YH₃, hydrogen deficiencies are required to serve as a catalytically active phase. The de/hydrogenation kinetics of dry-milled sample is fairly worse than that of Mg_{87.5}Ni_{5.5}Y₇ NPs (Supplementary Fig. S7). The dehydrogenation kinetics were analyzed using the JMAK model and the Arrhenius equation to determine the apparent activation energy, and the isothermal kinetics were further explored using the Sharp and Jones method (Supplementary Table S1).

The results revealed that Mg_{87.5}Ni_{5.5}Y₇ NPs achieved 5.15 wt.% H₂ released within 3 minutes at 300 °C, reaching 95 % of its theoretical capacity, and released 4.85 wt.% H₂ in 15 min at 240 °C (Fig. 3a). The analysis indicated its apparent activation energy of 69.9 kJ·mol⁻¹, significantly lower than 158.0 kJ·mol⁻¹ reported for bulk MgH₂ (Fig. 3g)⁵⁰. The isothermal kinetic analysis of Mg_{87.5}Ni_{5.5}Y₇ NPs showed that the experimental data were well fitted to the A2 model, suggesting that nucleation-and-growth of Mg/MgH₂ phases is the rate-determining step, consistent with previously reported Mg-TM-RE (TM = transition metals, RE=rare earths) hydrogen storage alloys (Supplementary Table S2 and Supplementary Fig. S10)¹⁹. These findings demonstrate that nanosizing Mg_{87.5}Ni_{5.5}Y₇ notably improves the dehydrogenation kinetics by increasing surface reactivity and reducing diffusion barriers, compared with the reported Mg-TM-RE systems (Fig. 3h and Supplementary Table S3)^{51–55}.

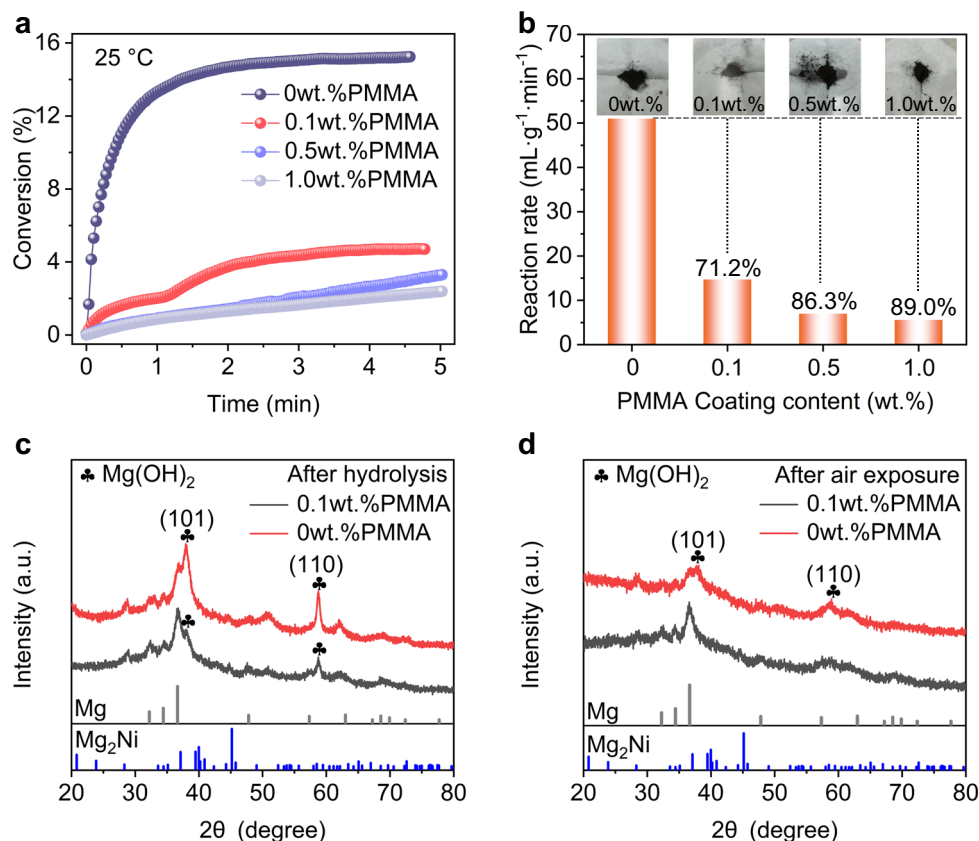


Fig. 2 | Surface durability of Mg_{87.5}Ni_{5.5}Y₇ NPs. **a Kinetic hydrogen generation via hydrolysis measured at room temperature. **b** Hydrogen generation rate in alloys with varied PMMA additions. The inset shows actual photographs of tested Mg_{87.5}Ni_{5.5}Y₇ NPs coated with different PMMA coatings. The samples were placed**

on weighing paper with a size of 9.8 cm × 9.8 cm. **c**, **d** compare the XRD data of uncoated and 0.1 wt.% PMMA coated Mg_{87.5}Ni_{5.5}Y₇ NPs after water and after two weeks of exposure to air. The reference peaks of Mg and Mg₂Ni were shown as gray and blue solid lines. The club symbol represents the peak position of Mg(OH)₂.

To explore the impacts of PMMA coating on dehydrogenation kinetics, we synthesized Mg_{87.5}Ni_{5.5}Y₇ NPs with varying PMMA thicknesses and tested their dehydrogenation capabilities from 240 °C and 300 °C. At 300 °C, 0.1-PMMA@Mg_{87.5}Ni_{5.5}Y₇ released 4.85 wt.% H₂, while 0.5-PMMA@Mg_{87.5}Ni_{5.5}Y₇ showed reduced capacity of 3.65 wt.% H₂, with 83.5 kJ·mol⁻¹ and 81.3 kJ·mol⁻¹, respectively (Fig. 3b–g). This temperature-dependent trend persisted at 240 °C, with desorption capacities decreasing to 4.46 wt.% and 3.61 wt.% H₂, respectively, maintaining the inverse correlation between PMMA loading and hydrogen release efficiency. The kinetic model was fitted to the R2 model (Supplementary Table S4 and Supplementary Fig. S11), indicating that interfacial chemical reactions are the rate-determining step. Accordingly, the PMMA layer on the alloy surface impeded hydrogen molecule access to active sites, thereby suppressing the interfacial reaction kinetics. The suppressed dehydrogenation kinetics corroborate this mechanism observed for 1.0-PMMA@Mg_{87.5}Ni_{5.5}Y₇. It only releases 1.94 wt.% H₂ at 300 °C and 1.76 wt.% H₂ at 240 °C. The excessive coating of 1.0 wt.% PMMA caused a 63.1% hydrogen capacity loss and a 28.0–52.8 % increase in the activation energy (Supplementary Fig. S12). Supplementary Fig. S13 shows the equilibrium pressures of uncoated and 0.1-PMMA@Mg_{87.5}Ni_{5.5}Y₇. The reaction enthalpy obtained from van't Hoff equation shows the nanosizing effect affect little to the thermodynamic properties.

To investigate the effects of different PMMA concentrations on the microstructure and surface chemical states of dehydrogenated Mg_{87.5}Ni_{5.5}Y₇ alloys, we systematically analyzed the dehydrogenated samples. All the samples predominantly consist of Mg, Mg₂Ni, and YH₃ phases after dehydrogenation (Supplementary Fig. S14). The YH₃ phase, formed during hydrogen absorption, remains stable without

decomposition during the dehydrogenation process. SEM images and EDS elemental mappings of dehydrogenated alloys confirm that the modified samples with varying PMMA concentrations maintain a fine particulate morphology after dehydrogenation (Supplementary Fig. S15). These results indicate that the Mg_{87.5}Ni_{5.5}Y₇ alloy maintains a relatively stable phase composition after dehydrogenation, and the different PMMA concentrations have minimal impact on the phase distribution.

HRTEM-EDS mapping (Supplementary Fig. S16) reveals uniform dispersion of Mg and Y elements, whereas Ni predominantly segregates as Mg₂Ni clusters within the alloy matrix after dehydrogenation. XPS analysis of uncoated and 0.1 wt.% PMMA-coated samples reveals that the Mg 1s spectra resolves dual peaks, i.e., a metallic magnesium component at 1303.5 eV and an oxidized magnesium species at 1306.3 eV (Supplementary Fig. S17). This indicates that partial surface oxidation exists. Meanwhile, the 0.5 and 1.0 wt.% PMMA samples show a single Mg 1s peak at 1303 eV, verifying complete dehydrogenation without detectable oxidation. The Ni 2p spectra consistently displays spin-orbit doublets (2p_{3/2} and 2p_{1/2}) accompanied by two characteristic satellite peaks across all compositions. The dominant 2p_{3/2} component at 852.5 eV corresponds to Mg–Ni intermetallic bonding, confirming the structural integrity of intermetallic phases during dehydrogenation. The Y 3d spectra reveals spin-orbit split 3d_{5/2} and 3d_{3/2} doublets, where the 3d_{5/2} peak at 157.2 eV is assigned to Y–H bonding configurations. Optimizing the concentration of PMMA is critical to balance surface protection with hydrogen storage performance. Based on our preliminary analysis of samples with varying PMMA contents, 0.1-PMMA@Mg_{87.5}Ni_{5.5}Y₇ exhibited an optimal combination of high hydrogen storage capacity and surface stability. Hence, we selected it

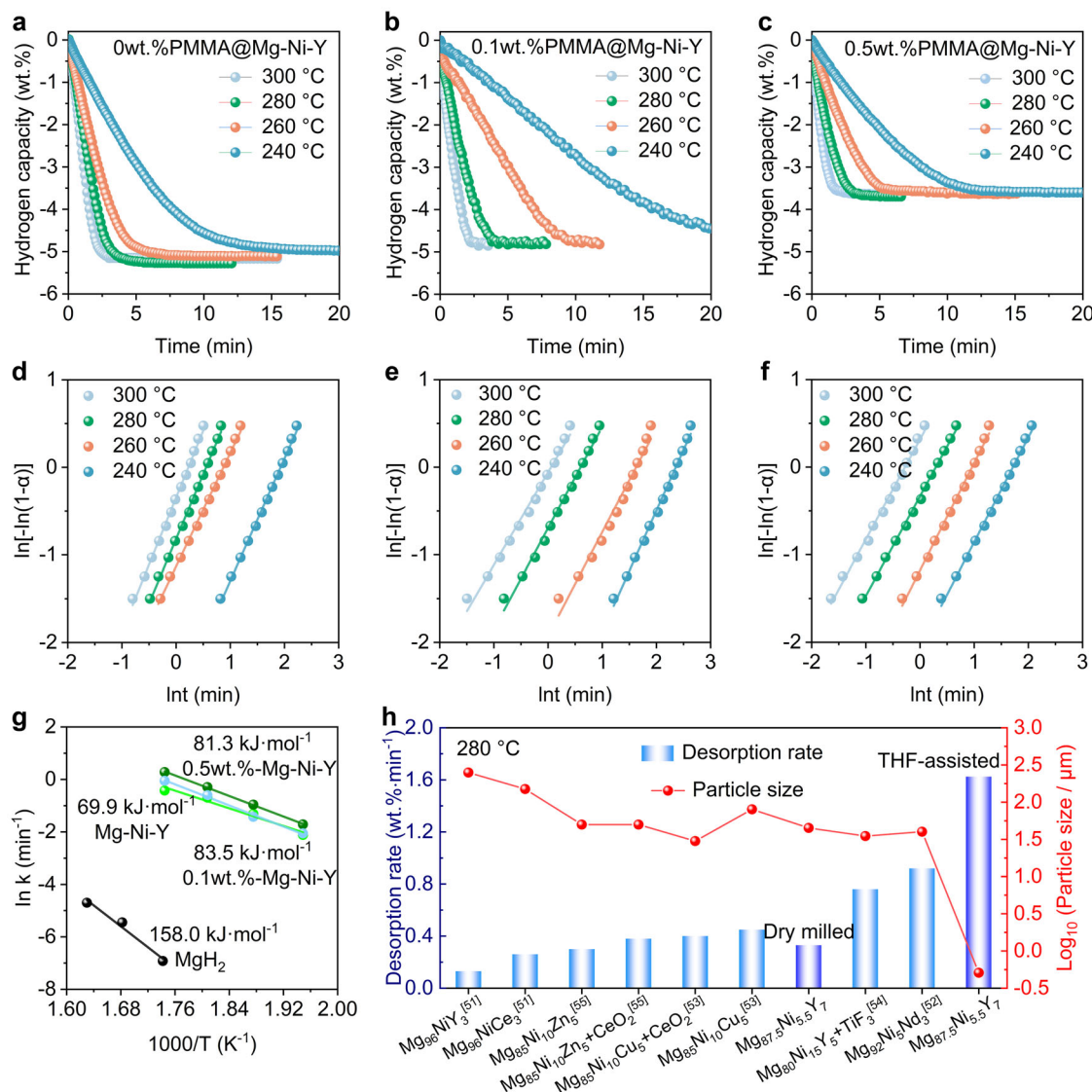


Fig. 3 | Hydrogen Storage properties. **a–c** Isothermal dehydrogenation kinetic curves of the nanostructured $\text{Mg}_{87.5}\text{Ni}_{5.5}\text{Y}_7$ alloy with three different PMMA protective layer contents. The isothermal dehydrogenation measurements were conducted under the initial pressure of 0.01 bar. **d–f** JMAK plots of corresponding kinetic data. **g** Arrhenius's plots obtained from JMAK plots. **h** Hydrogen desorption

performance comparison at 280 °C between the nanostructured $\text{Mg}_{87.5}\text{Ni}_{5.5}\text{Y}_7$ alloy developed in this work and other reported Mg-based alloys^{51–55}. The data of dry-milled and THF-assisted samples were drawn utilizing blue bars, while the reference data were illustrated utilizing light-blue bars, respectively. The red dots illustrate the mean particle size of the compared samples.

for in-depth characterization to further elucidate its cyclic hydrogen storage performance and structural stability.

The cycle stability of uncoated and 0.1-PMMA coated $\text{Mg}_{87.5}\text{Ni}_{5.5}\text{Y}_7$ NPs is presented in Fig. 4a. To each sample, cycle stability was evaluated up to 500 cycles. Both samples exhibit excellent cycling stability, while the uncoated $\text{Mg}_{87.5}\text{Ni}_{5.5}\text{Y}_7$ exhibits persistent degradation in terms of hydrogen storage capacity and reaction rates (Fig. 4a and b). After experiencing 500 cycles, the hydrogen storage capacity changed from 4.86 wt.% to 4.52 wt.%. Notable degradation of hydrogen storage capacity and reaction rates were not identified for the 0.1-PMMA coated $\text{Mg}_{87.5}\text{Ni}_{5.5}\text{Y}_7$ (Fig. 4a and b). The 0.1 wt.% PMMA-coated $\text{Mg}_{87.5}\text{Ni}_{5.5}\text{Y}_7$ material outperforms previously reported Mg-based systems in both de/hydrogenation kinetics and cycling stability (Fig. 4c)^{56–80}. These results collectively confirm that the PMMA-coated nanocrystalline alloy powder possesses exceptional chemical stability and remarkable cyclic durability under repeated hydrogen cycling conditions.

Figure 5a shows the Mg, Ni and Y XPS data of 50 and 500 times cycled uncoated $\text{Mg}_{87.5}\text{Ni}_{5.5}\text{Y}_7$ NPs. The Mg 1s spectrum exhibits a

metallic Mg^0 peak centered at 1303.5 eV, indicating minimal surface oxidation. The Ni 2p spectrum was deconvoluted into Mg–Ni alloy components with two satellite peaks, confirming the presence of Mg–Ni intermetallic bonding. The Y 3d spectrum revealed a Y–H bonding doublet, suggesting the presence of YH_3 species. These are consistent with XRD data of cycled samples (Supplementary Figs. S14 and S18), showing that the Mg, Mg₂Ni and YH_3 are the major phases for the dehydrogenated samples. It should be highlighted that the XPS data is largely unchanged between the 50th and 500th samples for the uncoated $\text{Mg}_{87.5}\text{Ni}_{5.5}\text{Y}_7$ NPs (Fig. 5a). These suggest that the degradation of hydrogen storage capability is likely associated with the structural or morphological evolution of materials. Figure 5b, c show the TEM images of uncoated and 0.1 wt.% PMMA-coated $\text{Mg}_{87.5}\text{Ni}_{5.5}\text{Y}_7$ NPs after 500 cycles. While the chemical composition keeps relatively uniform, clear particle growth can be identified for the uncoated $\text{Mg}_{87.5}\text{Ni}_{5.5}\text{Y}_7$ NPs relative to the 50th cycled sample (Supplementary Fig. S19), leading to the degraded cycle properties. Meanwhile, the 0.1 wt.% PMMA coated sample kept its finer particle morphology even after the long-cycle experiment (Fig. 5c). These data show that PMMA

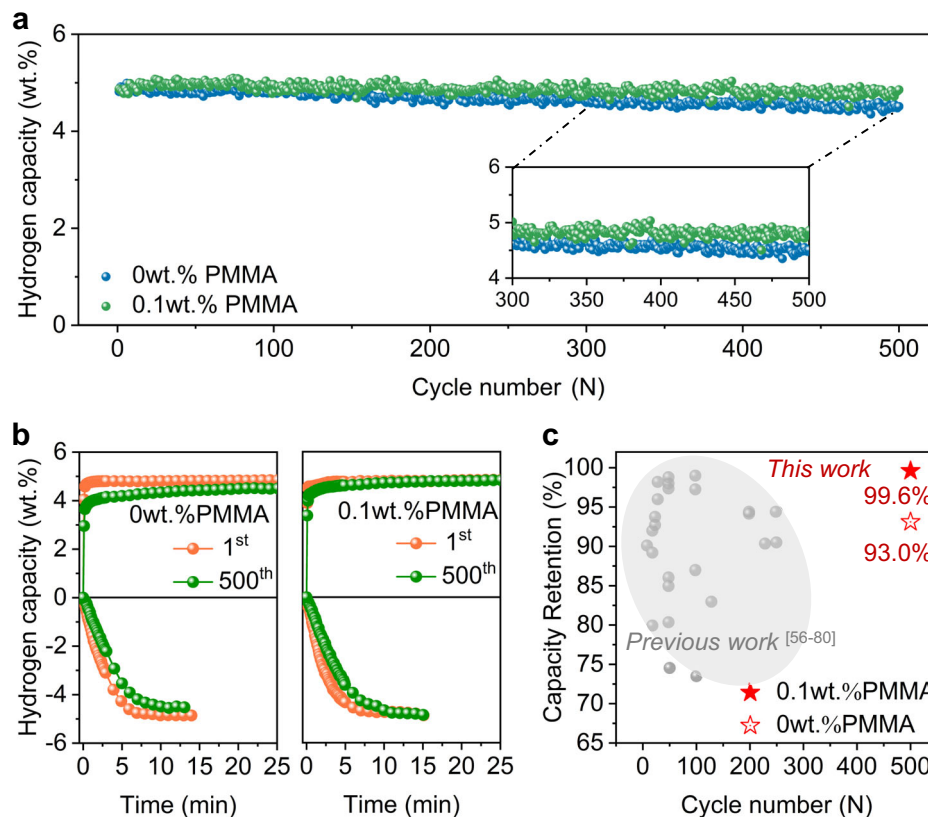


Fig. 4 | Cycle stability. **a** Cycle stability of uncoated and 0.1-PMMA coated $\text{Mg}_{87.5}\text{Ni}_{5.5}\text{Y}_7$ NPs. The hydrogenation and dehydrogenation reactions were conducted at 280 °C under 30 bar and 0.01 bar, respectively. The inset emphasizes the hydrogen storage capacity degradation tendency between PMMA uncoated (blue

dots) and 0.1 wt.% coated (green dots) samples. Evolution of their de/hydrogenation kinetics are shown in **(b)**. The **(c)** compares the cycle stability with other Mg-based hydrogen storage materials⁵⁶⁻⁸⁰.

coating not only improves chemical stability but also helpful to keep particle morphology during long-cycle operation.

Solvent-mediated partial ionicity

To elucidate the formation mechanism of nanostructures, we calculated the adsorption energies of THF at four distinct sites on the Mg (0001) surface, namely FCC-hollow, Bridge, HCP-hollow and on-top sites. Figure 6a shows that the most stable adsorption configuration occurs at the on-top site above Mg atoms, with an adsorption energy of -0.48 eV. Bader charge analysis (Fig. 6b and Supplementary Fig. S20) combined with charge distribution difference calculations reveal that upon THF adsorption, the Mg atom coordinating with the oxygen loses 0.56 electrons (manifested as positive charge states in blue), while neighboring Mg atoms acquire 0.03-0.08 electrons, giving rise to the $\text{Mg}^{\delta+}$ - $\text{Mg}^{\delta-}$ dipole structure. Additionally, Y-doping induces charge redistribution in proximal Mg atoms, with electron transfer quantities as quantified (Supplementary Fig. S21). Different views of the THF adsorption structure at the on-top site of Mg and the Y-doped structure are shown in Supplementary Fig. S22. Indeed, XPS analysis on the as milled samples show the presence of both positively and negatively charged Mg, consistent with the DFT calculations (Supplementary Fig. S23). The synergistic interplay between THF adsorption and Y-doping induces localized charge redistribution in adjacent Mg atoms, giving rise to the partial ionicity between Mg atoms.

Subsequently, we discuss the impact of cyclohexane adsorption on Mg-based alloy. Unlike THF, cyclohexane is characterized by less polarized molecules and exhibits much weaker interaction (Supplementary Figs. S24 and S25). As a result, adsorption of cyclohexane on Mg-alloy does not cause drastic charge redistribution as was observed

for THF, and this is why cyclohexane does not obviously contribute to mechanical nanosizing efficiency (Supplementary Fig. S4).

Such partial ionicity should suppress the ductility of Mg metal and maximize the ball milling-driven structural deformation that facilitates ion migration. The modified surface mechanical properties are indeed demonstrated utilizing Vickers hardness measurements. As shown in Fig. 6c and d, the notable enhancement of Vickers hardness was identified for the THF-adsorbed sample. It achieved an average hardness of 103.1 HV, representing 21.9 % enhancement compared to the untreated surface (84.6 HV) (Supplementary Table S5). These results indicate that the Mg surface becomes less ductile and thus more susceptible to mechanical impact, leading to enhanced ball-milling efficiency. Based on the above-mentioned results, we propose the mechanism of solvent-assisted mechanical nanosizing processes in Fig. 6e. First, solvent molecules, such as THF, adsorb on the metal surface. It gives rise to an electron distribution that enhances surface hardness, making the metal powder more susceptible to mechanical impact. Subsequently, the cracks are easier to generate, and the solvent molecules can be adsorbed on the fresh surface, further enabling mechanical nanosizing.

In summary, we successfully prepared $\text{Mg}_{87.5}\text{Ni}_{5.5}\text{Y}_7$ NPs utilizing solvent-assisted mechanical ball-milling. It was found that the adsorption of solvents, such as THF, induces weak positive and negative charge distribution on the Mg surface. This partial ionicity enhances the surface hardness of Mg-based alloys, thereby enhancing mechanical nanosizing effect by the factor of 88. The nanostructured $\text{Mg}_{87.5}\text{Ni}_{5.5}\text{Y}_7$ alloy exhibited exceptional dehydrogenation kinetics, releasing 5.22 wt.% H_2 within 5 min at 280 °C and 4.85 wt.% H_2 in 15 min even at 240 °C, exceeding previously reported Mg-based hydrogen storage alloys. The $\text{Mg}_{87.5}\text{Ni}_{5.5}\text{Y}_7$ NPs also exhibit improved chemical

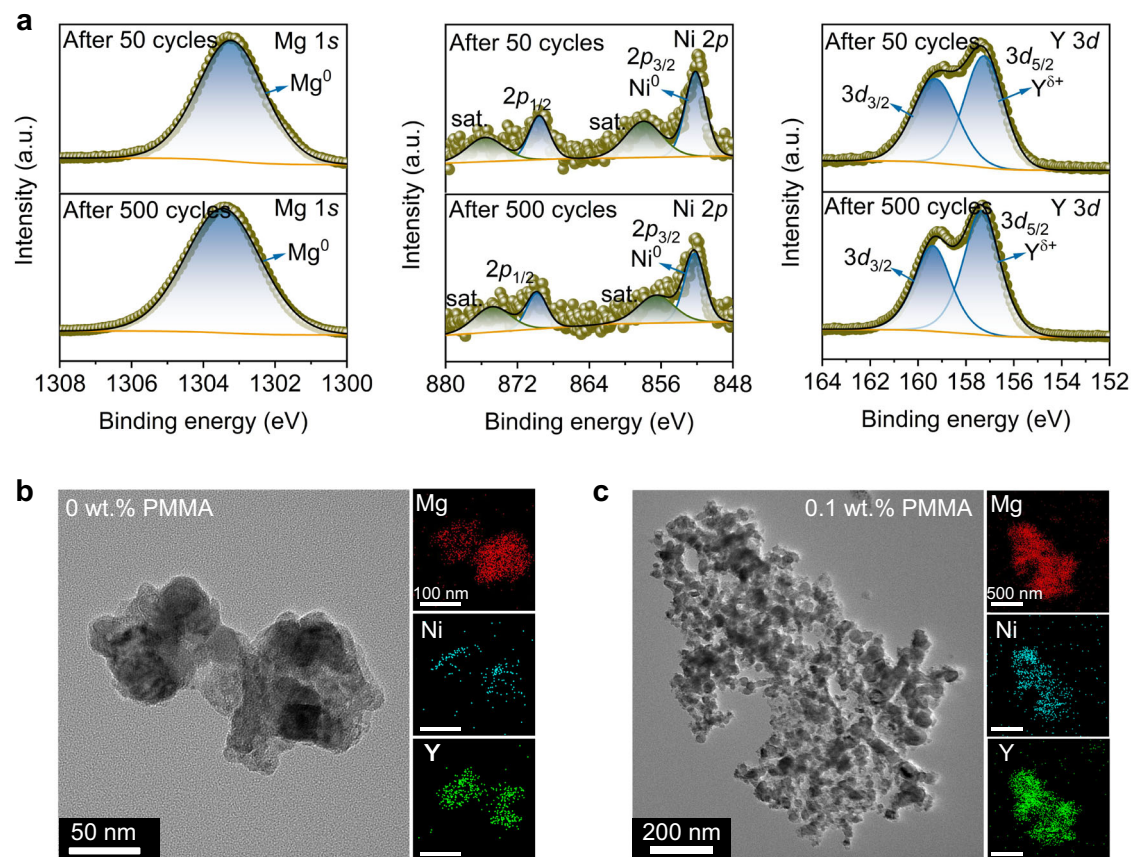


Fig. 5 | Chemical and structural evolution. **a** The XPS data of 50 and 500 times cycled $\text{Mg}_{87.5}\text{Ni}_{5.5}\text{Y}_7$ NPs. The dots and solid lines represent experimental data and data fitting. During the fitting of the Mg 1s, Ni 2p, and Y 3d core-level spectra, the full width at half maximum (FWHM) was constrained to be identical for multiple

peaks belonging to the same chemical state. Their area ratios (shaded region) were also fixed to the theoretical value. **b, c** TEM-EDS data of 500-cycled uncoated $\text{Mg}_{87.5}\text{Ni}_{5.5}\text{Y}_7$ and 0.1-PMMA@ $\text{Mg}_{87.5}\text{Ni}_{5.5}\text{Y}_7$ NPs. The red, light-blue and green dots in the EDS represent Mg, Ni and Y signals, respectively.

and cycle stability, which is further improved by PMMA coating. Notable kinetic and capacity degradation were not identified for the PMMA-coated $\text{Mg}_{87.5}\text{Ni}_{5.5}\text{Y}_7$ NPs, at least for 500 cycles. The present data reveals how the charge rearrangement caused by metal-solvent interfaces affect surface mechanical properties and improve nanofabrication efficiency of ball-milling, which is even applicable to ductile Mg-based alloys, offering an affordable and scalable approach for nanofabrication of inorganic materials.

Methods

Sample preparation

The $\text{Mg}_{87.5}\text{Ni}_{5.5}\text{Y}_7$ alloy was synthesized via vacuum induction melting under a high-purity argon atmosphere. Nanostructured alloy powder was fabricated via solvent-assisted ball milling with the following protocol. In it, 0.25 g of alloy powder was weighed into a 100 ml ball milling jar, followed by uniform dispersion of 1 mL tetrahydrofuran (THF) onto the powder surface using a calibrated micropipette. Ball milling was performed for 20 hours under an argon atmosphere. During the ball-milling, ball-to-powder ratio was set to 40:1 with the rotational speed of 400 rpm. 10 min pause was introduced between every 10 min milling to prevent overheating.

Three polymethyl methacrylate (PMMA, Mw - 120,000, Aladdin, Shanghai) solutions with distinct concentrations (0.00025 g/mL, 0.00125 g/mL, 0.0025 g/mL) were prepared by dissolving 0.005 g, 0.025 g, and 0.050 g PMMA in 20 mL anhydrous tetrahydrofuran (99.5%, Macklin). The mixtures were magnetically stirred in argon-protected containers for 12 h to ensure complete dissolution. Three gradient-concentration PMMA solutions were mixed with the $\text{Mg}_{87.5}\text{Ni}_{5.5}\text{Y}_7$ NPs for PMMA coating. The experimental parameters are

summarized in Supplementary Table S6. For the test of cyclohexane-assisted ball-milling the solvent was changed to cyclohexane (99.9 %, Macklin) while other conditions were retained.

Material characterization

The phase composition of the alloy was characterized by X-ray diffraction (XRD, Rigaku, Cu K α radiation) at a step size of 0.02° and a scanning rate of 5°·min⁻¹. The morphological characteristics and elemental distribution of the samples were analyzed before and after hydrogen storage performance tests using environmental scanning electron microscopy (ESEM, Quattro S) and transmission electron microscopy (TEM; Talos F200S). The error bars of particle distribution were estimated utilizing Gaussian fit with statistics from $n = 147$. The elemental composition and stoichiometry of the samples were determined by X-ray photoelectron spectroscopy (XPS, Thermo K-Alpha, Thermo Fisher Scientific). The C 1s peak (284.8 eV) was used as the reference. During the fitting of the Mg 1s, Ni 2p, and Y 3d core-level spectra, the full width at half maximum (FWHM) was constrained to be identical for multiple peaks belonging to the same chemical state, and their area ratios were fixed. For the Ni 2p and Y 3d doublet, the area ratio and splitting set at reference values, thereby ensuring the accuracy of the results.

Vickers hardness testing using a 300 g load and a holding time of 10 s was carried out on a Micro Vickers hardness testing system (UHV-1000F). For each sample, 120 tests were performed and utilized for statics estimation, such as median/mean values, the 25th/75th quartiles and standard deviation. Prior to the Vickers hardness test, the alloys surface was polished. THF was then sprayed to the surface, and the excess THF was dried under an ambient condition.

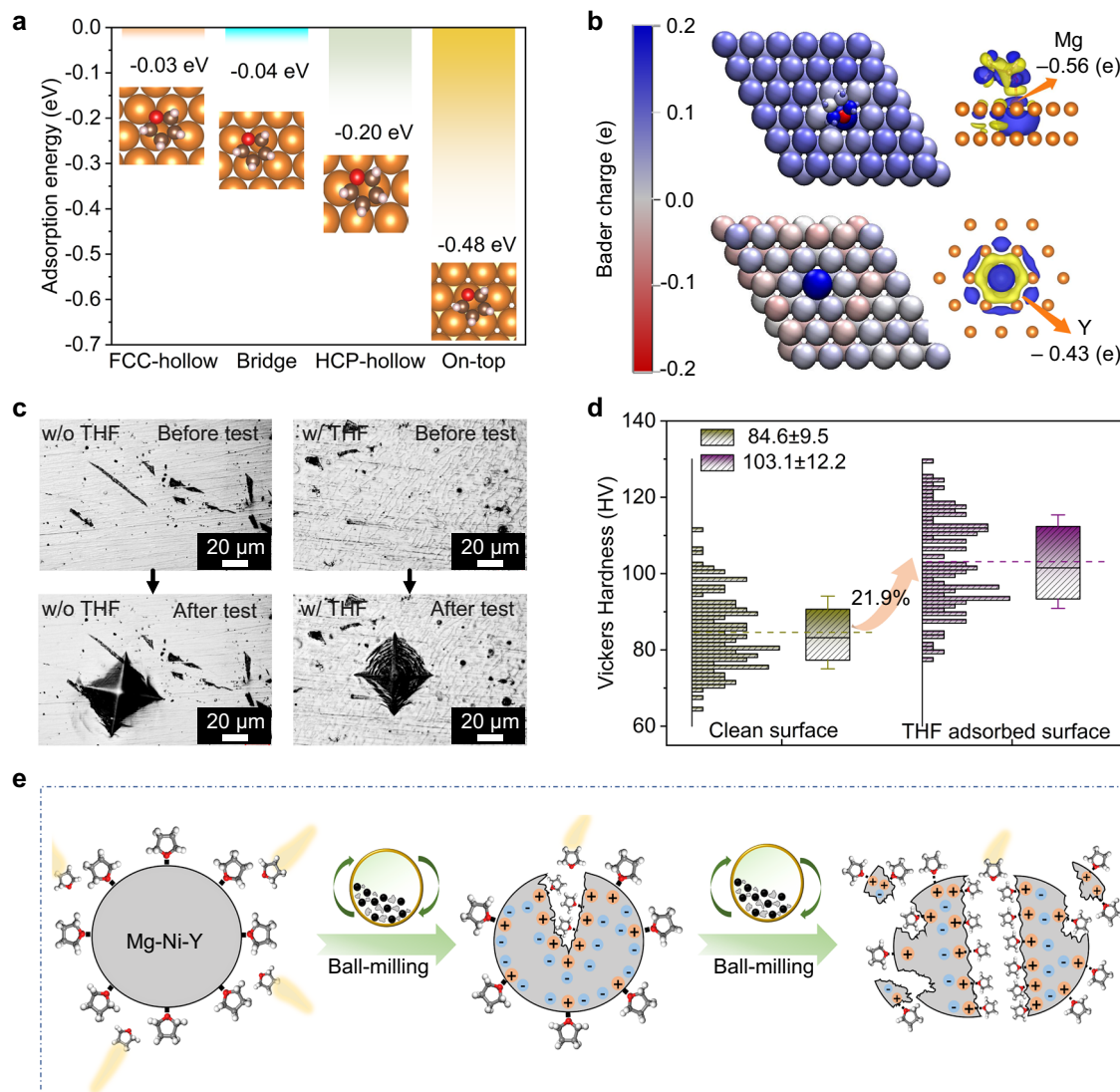


Fig. 6 | Partial ionicity-mediated nanosizing effect. **a** Calculated adsorption energies of THF at four different sites on the Mg (0001) surface. **b** Bader charge analysis and charge density difference analysis, along with the differential charge density analysis, with accompanying visualizations of the top view of THF on Mg and the top view of the Y-doped structure. **c** The microstructure of studied $\text{Mg}_{87.5}\text{Ni}_{5.5}\text{Y}_7$ alloy before and after Vickers hardness test. Both clean surface and THF-adsorbed surface were tested. **d** The summary of the Vickers hardness test. For

each sample, 120 tests were performed and utilized for statics evaluation. The box plot depicts the median (solid line), mean (dashed line), the 25th and 75th quartiles (box), respectively. Error bars were derived from the standard deviation.

e Proposed solvent-assisted mechanical nanosizing mechanism. It is considered that the adsorbed THF gives rise to electron distribution on Mg surface. It resulted in harder surface properties and made the Mg-based alloy being more susceptible to mechanical impact.

Hydrolysis corrosion experiments

The hydrolysis corrosion reaction was tested in a hydrolysis H_2 generation device based on the drainage method. The equipment consists of a reaction device and a data logger. The amount of gas released was measured by the mass of water discharged from the gas scrubber bottle, which was weighed with a balance throughout. The weight of deionized water was obtained automatically by an electronic balance connected to a computer, which stored data and reaction times. Then, the generation rate-time curve corresponding to the hydrolysis H_2 generation process was obtained. For hydrolysis corrosion reaction, in a typical experiment, ~0.05 g of the sample was loaded in a 100 ml flask bottle, and 50 ml deionized water was added to start the reaction at room temperature and under ambient atmosphere. The flask was immersed in a circulating water bath to control reaction temperature and put over a magnetic stirrer to agitate the reactions. The background flow ($0.15 \text{ ml} \cdot \text{min}^{-1}$) was subtracted from the data.

Hydrogen storage performance measurements

The isothermal hydrogenation and dehydrogenation characteristics of the samples, including cycling curves, were investigated using a commercial Sieverts-type apparatus (PCT Pro, Setaram and H-Sorb 4600PCT PRO, Ciqtec). The background hydrogen pressures were set to 30 bar for hydrogenation and 0.01 bar for dehydrogenation processes, respectively. Prior to hydrogen absorption/desorption kinetics testing, the alloy samples were subjected to 5 activation cycles at 300 °C.

To better understand the dehydrogenation kinetic behavior, the equations associated with Sharp's and Jone's method model (equation 1 and 2) were used to fit the isothermal dehydrogenation curves at different temperatures^{81,82}

$$d_{\alpha}/d_t = kf(\alpha) \quad (1)$$

$$f(\alpha) = A(t/t_{0.5}) \quad (2)$$

where d_α is the differential of conversion extent, d_t is the differential of time, k is the reaction rate constant, $f(\alpha)$ is a function that depends on a specific kinetic mechanism, A represents a constant related to the kinetic mechanism, and $t_{0.5}$ represents the time when α equals to 0.5. The kinetic model was obtained by plotting the experimental value $(t/t_{0.5})_{\text{exp}}$ against the theoretical value $(t/t_{0.5})_{\text{theo}}$.

The PCT curves of samples in different cycle stages were tested at a temperatures of 280 °C, 300 °C, 320 °C, 340 °C and hydrogen pressures ranging from 0.02 to 3 MPa. The reaction enthalpy (ΔH) was then calculated utilizing van't Hoff equation.

$$\ln\left(\frac{P_{\text{H}_2}}{P_0}\right) = \Delta H/RT - \Delta S/R \quad (3)$$

where P_{H_2} denotes the equilibrium pressure of the Mg/MgH₂ reaction, ΔH represents the enthalpy change, ΔS is the entropy change, T is the testing temperature, R is the gas constant [8.314 J/(mol·K)], and P_0 the standard atmospheric pressure ($\sim 1.01 \times 10^5$ Pa).

DFT studies

All structural relaxations and electronic structure calculations were carried out using density functional theory (DFT) as implemented in the Vienna Ab initio Simulation Package (VASP)⁸³. Based on the optimized bulk lattice parameters, a 6×6 Mg(0001) surface model was constructed for the simulations, with a vacuum layer of 15 Å introduced to eliminate interlayer interactions. The supercell consists of five atomic layers, with the bottom three layers fixed to mimic the bulk behavior and improve computational efficiency. During geometry optimization, the plane-wave cutoff energy was set to 450 eV, and a Monkhorst-Pack k-point mesh of $5 \times 5 \times 1$ was used. The convergence criteria for electronic self-consistent iteration and ionic relaxation were set to 10^{-6} eV per atom for the total energy and $0.01 \text{ eV} \cdot \text{Å}^{-1}$ for the maximum atomic force, respectively. The exchange-correlation functional was treated within the generalized gradient approximation (GGA) using the Perdew-Burke-Ernzerhof (PBE) formulation^{84–86}. The electron charge density was analyzed using the Bader charge analysis method combined with charge density difference calculations. For the transition state analysis of the hydrogen dissociation reaction, the climbing image nudged elastic band (CI-NEB) was employed to identify saddle points and minimum energy paths (MEPs)^{87,88}. The number of CI-NEB images was determined using the VASP-VTST⁹⁷⁸ script, based on the interatomic distances between the initial and final states. All transition-state models were fully optimized until the energy and force convergence thresholds of 1×10^{-6} eV and $0.01 \text{ eV} \cdot \text{Å}^{-1}$, respectively, were reached. The adsorption energy $E_{\text{ad}}(\text{X})$ of X (X = tetrahydrofuran or cyclohexane) on the surface is defined as $E_{\text{ad}}(\text{X}) = E_{\text{tot}}(\text{X}/\text{sub}) - E(\text{sub}) - E(\text{X})$, where $E_{\text{tot}}(\text{X}/\text{sub})$ is the total energy of the optimized configuration of the X molecule adsorbed on the substrate, $E(\text{sub})$ is the total energy of the clean substrate, and $E(\text{X})$ is the total energy of an isolated X molecule.

Data availability

The data generated in this study are presented in the main text, Supplementary Information and Source Data file. Source data are provided in this paper.

References

- Allendorf, M. D. et al. Challenges to developing materials for the transport and storage of hydrogen. *Nat. Chem.* **14**, 1214–1223 (2022).
- Guan, H., Liu, J., Li, Q., Lu, Y. & Pan, F. Chemically stable TMO @Ti-MgO (TM = Mn and Cu) catalyst enhanced De/hydrogenation kinetics of Mg/MgH₂. *J. Magnes. Alloys* <https://doi.org/10.1016/j.jma.2025.02.032> (2025).
- Guan, H. et al. Titanium-nickel dual active sites enabled reversible hydrogen storage of magnesium at 180 °C with exceptional cycle stability. *Adv. Mater.* **37**, 2500178 (2025).
- Jeon, K.-J. et al. Air-stable magnesium nanocomposites provide rapid and high-capacity hydrogen storage without using heavy-metal catalysts. *Nat. Mater.* **10**, 286–290 (2011).
- Kim, H. et al. Facile synthesis of nanoporous Mg crystalline structure by organic solvent-based reduction for solid-state hydrogen storage. *Nat. Commun.* **15**, 10800 (2024).
- Larsson, P., Araújo, C. M., Larsson, J. A., Jena, P. & Ahuja, R. Role of catalysts in dehydrogenation of MgH₂ nanoclusters. *Proc. Natl. Acad. Sci. USA* **105**, 8227–8231 (2008).
- Li, Q. et al. Thermodynamics and kinetics of hydriding and dehydriding reactions in Mg-based hydrogen storage materials. *J. Magnes. Alloys* **9**, 1922–1941 (2021).
- Wang, H. et al. Thermodynamic and kinetic regulation for Mg-based hydrogen storage materials: challenges, strategies, and perspectives. *Adv. Funct. Mater.* **34**, 2406639 (2024).
- Zhang, X. et al. Atomic reconstruction for realizing stable solar-driven reversible hydrogen storage of magnesium hydride. *Nat. Commun.* **15**, 2851 (2024).
- Zhao, X. et al. Tunable metal-hydrogen bonding in Cu-Ru catalysts enables selective hydrogen storage reactions in Mg-based composite. *Adv. Funct. Mater.* **35**, 2505352 (2025).
- Han, Z., Wu, Y., Yu, H. & Zhou, S. Location-dependent effect of nickel on hydrogen dissociation and diffusion on Mg (0001) surface: Insights into hydrogen storage material design. *J. Magnes. Alloys* **10**, 1617–1630 (2022).
- Xinglin, Y., Xiaohui, L., Jiaqi, Z., Quanhui, H. & Junhu, Z. Progress in improving hydrogen storage properties of Mg-based materials. *Mater. Today Adv.* **19**, 100387 (2023).
- Chen, Y. et al. Hydrogen Storage in Mg-Ni-Type Alloys with La and Sm Incorporation. *ACS Appl. Energy Mater.* **7**, 8858–8868 (2024).
- Liang, G. Y., Wu, D. C., Li, L. & Huang, L. J. A discussion on decay of discharge capacity for amorphous Mg-Ni-Nd hydrogen storage alloy. *J. Power Sources* **186**, 528–531 (2009).
- Liu, J. W., Zou, C. C., Wang, H., Ouyang, L. Z. & Zhu, M. Facilitating de/hydrogenation by long-period stacking ordered structure in Mg based alloys. *Int. J. Hydrogen Energy* **38**, 10438–10445 (2013).
- Yin, J., Yamada, T., Yoshinari, O. & Tanaka, K. Improvement of hydrogen storage properties of Mg-Ni alloys by rare-earth addition. *Mater. Trans.* **42**, 712–716 (2001).
- Li, Y., Gu, Q., Li, Q. & Zhang, T. In-situ synchrotron X-ray diffraction investigation on hydrogen-induced decomposition of long period stacking ordered structure in Mg-Ni-Y system. *Scr. Mater.* **127**, 102–107 (2017).
- Luo, Q. et al. Achieving superior cycling stability by in situ forming NdH₂-Mg-Mg₂Ni nanocomposites. *J. Mater. Chem. A* **6**, 23308–23317 (2018).
- Sun, X. et al. Hot extrusion-induced Mg-Ni-Y alloy with enhanced hydrogen storage kinetics. *J. Mater. Sci. Technol.* **202**, 119–128 (2024).
- Spassov, T., Rangelova, V. & Neykov, N. Nanocrystallization and hydrogen storage in rapidly solidified Mg-Ni-RE alloys. *J. Alloys Compounds* **334**, 219–223 (2002).
- Tanaka, K. et al. Improvement of hydrogen storage properties of melt-spun Mg-Ni-RE alloys by nanocrystallization. *J. Alloys Compounds* **293–295**, 521–525 (1999).
- Li, K., Huang, T., Gao, Y. & Zhou, C. Enhancing antioxidant properties of hydrogen storage alloys using PMMA coating. *Int. J. Hydrogen Energy* **48**, 4339–4348 (2023).
- Ranjbar, A. et al. Comparison of hydrogen storage properties of Mg-Ni from different preparation methods. *Mater. Chem. Phys.* **127**, 405–408 (2011).

24. Yu, X., Tang, Z., Sun, D., Ouyang, L. & Zhu, M. Recent advances and remaining challenges of nanostructured materials for hydrogen storage applications. *Prog. Mater. Sci.* **88**, 1–48 (2017).
25. Zhou, C. et al. In situ formation of nanocrystalline MgH₂ through room temperature hydrogenation. *Mater. Des.* **218**, 110729 (2022).
26. Rolison, D. R. et al. Multifunctional 3D nanoarchitectures for energy storage and conversion. *Chem. Soc. Rev.* **38**, 226–252 (2009).
27. Xu, C. et al. Graphene-based electrodes for electrochemical energy storage. *Energy Environ. Sci.* **6**, 1388–1414 (2013).
28. Zhou, Z.-Y., Tian, N., Li, J.-T., Broadwell, I. & Sun, S.-G. Nanomaterials of high surface energy with exceptional properties in catalysis and energy storage. *Chem. Soc. Rev.* **40**, 4167–4185 (2011).
29. Zhu, W. et al. Nanoconfined and in situ catalyzed MgH₂ self-assembled on 3D Ti₃C₂ MXene folded nanosheets with enhanced hydrogen sorption performances. *ACS Nano* **15**, 18494–18504 (2021).
30. Li, W., Li, C., Ma, H. & Chen, J. Magnesium nanowires: enhanced kinetics for hydrogen absorption and desorption. *J. Am. Chem. Soc.* **129**, 6710–6711 (2007).
31. Norberg, N. S., Arthur, T. S., Fredrick, S. J. & Prieto, A. L. Size-Dependent hydrogen storage properties of Mg nanocrystals prepared from solution. *J. Am. Chem. Soc.* **133**, 10679–10681 (2011).
32. Qin, J. et al. Construction of Mg/Zr superlattice structure to achieve efficient hydrogen storage via atomic-scale interaction in Mg-Zr modulation films. *Acta Materialia* **263**, 119470 (2024).
33. Zhang, X. et al. Realizing 6.7 wt% reversible storage of hydrogen at ambient temperature with non-confined ultrafine magnesium hydrides. *Energy Environ. Sci.* **14**, 2302–2313 (2021).
34. Banrejee, S., Kumar, A., Ruz, P. & Sudarsan, V. Improvement of hydrogen storage characteristics of catalyst free magnesium nanoparticles prepared by wet milling. *Int. J. Energy Res.* **45**, 17597–17608 (2021).
35. Cui, J. et al. Remarkable enhancement in dehydrogenation of MgH₂ by a nano-coating of multi-valence Ti-based catalysts. *J. Mater. Chem. A* **1**, 5603–5611 (2013).
36. Gao, G. et al. Improvement on hydrogen storage performance of MgH₂ by THF-promoted nano-crystallization under low-speed ball milling. *Rare Metals* **44**, 6366–6374 (2025).
37. Paik, B. et al. Evolution of microstructure in MgH₂ powder particles during high energy ball milling and hydrogen cycling. *J. Alloys Compounds* **492**, 515–520 (2010).
38. Porcheddu, A., Cincotti, A. & Delogu, F. Kinetics of MgH₂ formation by ball milling. *Int. J. Hydrogen Energy* **46**, 967–973 (2021).
39. Schimmel, H. G. et al. Structural information on ball milled magnesium hydride from vibrational spectroscopy and ab-initio calculations. *J. Alloys Compounds* **393**, 1–4 (2005).
40. Tian, M. & Shang, C. Nano-structured MgH₂ catalyzed by TIC nanoparticles for hydrogen storage. *J. Chem. Technol. Biotechnol.* **86**, 69–74 (2011).
41. Varin, R. A., Czujko, T., Chiu, C. & Wronski, Z. Particle size effects on the desorption properties of nanostructured magnesium dihydride (MgH₂) synthesized by controlled reactive mechanical milling (CRMM). *J. Alloys Compounds* **424**, 356–364 (2006).
42. Zou, R. et al. One-step synthesis of light metal nanoparticle from metastable complex. *Small* **19**, 2206518 (2022).
43. Zhang, T., Song, W., Kou, H. & Li, J. Surface valence transformation during thermal activation and hydrogenation thermodynamics of Mg-Ni-Y melt-spun ribbons. *Appl. Surface Sci.* **371**, 35–43 (2016).
44. Zhou, H. et al. Enhancement of hydrogen storage properties from amorphous Mg₈₅Ni₅Y₁₀ alloy. *J. NonCrystalline Solids* **605**, 122167 (2023).
45. Guan, H. et al. Dipole Coupling Accelerated H₂O Dissociation by Magnesium-Based Intermetallic Catalysts. *Angew. Chem. Int. Ed.* **63**, e202400119 (2024).
46. Hashimoto, T. & Notomi, M. Hydrogen storage properties of Mg-based multilayer films. *Mech. Eng. J.* **3**, 16-00228 (2016).
47. Shen, C. & Aguey-Zinsou, K.-F. Electrochemical deposited Mg-PPy multilayered film to store hydrogen. *Int. J. Hydrogen Energy* **43**, 22385–22390 (2018).
48. Yao, L. et al. Improved dehydrogenating property of poly-vinylpyrrolidone coated Mg-Ni hydrogen storage nano-composite prepared by hydriding combustion synthesis and wet mechanical milling. *Prog. Nat. Sci. Mater. Int.* **28**, 7–14 (2018).
49. Yuan, J. G., Zhu, Y. F., Li, L. Q., Wu, Y. & Zhou, S. X. Preparation and hydrogen storage property of Mg-based hydrogen storage composite embedded by polymethyl methacrylate. *Int. J. Hydrogen Energy* **42**, 22366–22372 (2017).
50. Guan, H. et al. Microscopic Scaling Relation of Ti-Based Catalysts in De/Hydrogenation Reactions of Mg/MgH₂. *ACS Catal.* **14**, 17159–17170 (2024).
51. Chen, Y. et al. Investigation of microstructure characteristics, kinetics, and thermodynamics of Mg-Ni-RE (RE = Y and RE = Ce) hydrogen storage alloys. *Int. J. Hydrogen Energy* **69**, 1329–1340 (2024).
52. Lin, M. et al. Hydrogen storage properties of Mg_{95-x}Ni₅Nd_x (x=0, 1, 3, 5) alloys. *Int. J. Hydrogen Energy* **97**, 11–24 (2025).
53. Yin, Y., Li, B., Yuan, Z., Qi, Y. & Zhang, Y. Enhanced hydrogen storage performance of Mg-Cu-Ni system catalyzed by CeO₂ additive. *J. Rare Earths* **38**, 983–993 (2020).
54. Yong, H. et al. In-situ influence of TiF₃ catalyst on the hydrogen storage behavior of Mg-Ni-Y based alloy. *J. Energy Storage* **77**, 110022 (2024).
55. Yuan, Z. et al. Influence of CeO₂ nanoparticles on microstructure and hydrogen storage performance of Mg-Ni-Zn alloy. *Mater. Charact.* **178**, 111248 (2021).
56. Chen, Y. et al. Mn nanoparticles enhanced dehydrogenation and hydrogenation kinetics of MgH₂ for hydrogen storage. *Trans. Non-ferrous Met. Soc. China* **31**, 3469–3477 (2021).
57. Ding, S. et al. A novel carbon-induced-porosity mechanism for improved cycling stability of magnesium hydride. *J. Magnes. Alloys* **13**, 1341–1352 (2025).
58. Fu, H. et al. Synergistic effect of a facilely synthesized MnV₂O₆ catalyst on improving the low-temperature kinetic properties of MgH₂. *ACS Appl. Mater. Interfaces* **14**, 33161–33172 (2022).
59. Guo, F., Zhang, T., Shi, L. & Song, L. Hydrogen absorption/desorption cycling performance of Mg-based alloys with in-situ formed Mg₂Ni and LaH_x (x=2, 3) nanocrystallines. *J. Magnes. Alloys* **11**, 1180–1192 (2023).
60. Guo, Z. et al. Catalytic phase engineering for enhanced hydrogen storage kinetics in Mg-Ni-Y-Si alloys via solid-solution and reprecipitation. *J. Alloys Compounds* **1030**, 180903 (2025).
61. Kajiwara, K., Sugime, H., Noda, S. & Hanada, N. Fast and stable hydrogen storage in the porous composite of MgH₂ with Nb₂O₅ catalyst and carbon nanotube. *J. Alloys Compounds* **893**, 162206 (2022).
62. Lan, Z. et al. Roles of in situ-formed NbN and Nb₂O₅ from N-doped Nb₂C MXene in regulating the re/hydrogenation and cycling performance of magnesium hydride. *Chem. Eng. J.* **431**, 133985 (2022).
63. Li, B. et al. Synchronously upgrading of hydrogen storage thermodynamic, kinetics and cycling properties of MgH₂ via VTiMn catalyst. *Sep. Purif. Technol.* **355**, 129760 (2025).
64. Li, H. et al. Effect of element substitution on hydrogen storage properties of La-Mg-Ni-based alloys prepared by heat treatment. *Intermetallics* **184**, 108861 (2025).
65. Li, J. et al. In situ formed MgTi₂O₄ from MgO improving the cycling stability of MgH₂. *Chem. Eng. J.* **470**, 144259 (2023).
66. Nyahuma, F. M. et al. Significantly improved hydrogen storage behaviors in MgH₂ with Nb nanocatalyst. *Int. J. Miner. Metall. Mater.* **29**, 1788–1797 (2022).

67. Peng, C., Li, Y. & Zhang, Q. Enhanced hydrogen desorption properties of MgH₂ by highly dispersed Ni: The role of in-situ hydrolysis of nickelocene in ball milling process. *J. Alloys Compounds* **900**, 163547 (2022).
68. Qin, Y. et al. Constructing VO/V₂O₃ interface to enhance hydrogen storage performance of MgH₂. *J. Magnes. Alloys* **12**, 4877–4886 (2024).
69. Ren, L. et al. Boosting hydrogen storage performance of MgH₂ by oxygen vacancy-Rich H-V₂O₅ nanosheet as an excited H-Pump. *NanoMicro Lett.* **16**, 160 (2024).
70. Sun, S. et al. Tailoring hydrogen storage properties in cold rolled Mg-Ni-Si alloys: Microstructural evolution and low-temperature performance optimization. *Chem. Eng. J.* **521**, 166822 (2025).
71. Tan, D., Peng, C. & Zhang, Q. Microstructural characteristics and hydrogen storage properties of the Mg-Ni-TiS₂ nanocomposite prepared by a solution-based method. *Int. J. Hydrogen Energy* **48**, 16756–16768 (2023).
72. Tanaka, H. et al. Cycle durability of Ca-Mg-Ni alloys and factors which cause degradation of hydrogen storage capacity. *Mater. Sci. Eng. B* **108**, 81–90 (2004).
73. Verma, S. K., Abu Shaz, M. & Yadav, T. P. Introducing 2D layered WS₂ and MoS₂ as an active catalyst to enhance the hydrogen storage properties of MgH₂. *Int. J. Hydrogen Energy* **87**, 1035–1046 (2024).
74. Xian, K. et al. A unique nanoflake-shape bimetallic Ti-Nb oxide of superior catalytic effect for hydrogen storage of MgH₂. *Small* **18**, 2107013 (2022).
75. Yang, J. et al. MXene-supported V₂O₅ nanocatalysts: Boosting hydrogen storage efficiency in MgH₂ through synergistic catalysis. *J. Energy Storage* **130**, 117474 (2025).
76. Zhang, H. et al. Engineering the oxygevacancies in Na₂Ti₃O₇ for boosting its catalytic performance in MgH₂ hydrogen storage. *ACS Sustain. Chem. Eng.* **10**, 363–371 (2021).
77. Zhang, J. et al. Single-atom Ni supported on TiO₂ for catalyzing hydrogen storage in MgH₂. *J. Am. Chem. Soc.* **146**, 10432–10442 (2024).
78. Zhang, Z. et al. Improving the hydrogen storage property of Sm_{6.5}Mg_{93.5}TiMn₂ by accelerating H₂ dissociation/recombination and H diffusion. *ACS Sustain. Chem. Eng.* **12**, 17702–17712 (2024).
79. Zhou, X. et al. The anionic Tx defects of Nb₂CT_x MXene as the effective catalytically active center for the Mg-based hydrogen storage materials. *J. Magnes. Alloys* **13**, 571–582 (2025).
80. Zou, R. et al. Enhancing the cycling stability of MgH₂ using nitrogen modified titanate. *J. Mater. Chem. A* **11**, 11748–11754 (2023).
81. Jones, L. F., Dollimore, D. & Nicklin, T. Comparison of experimental kinetic decomposition data with master data using a linear plot method. *Thermochimica Acta* **13**, 240–245 (1975).
82. Sharp, J. H., Brindley, G. W. & Achar, B. N. N. Numerical data for some commonly used solid state reaction equations. *J. Am. Ceramic Soc.* **49**, 379–382 (1966).
83. Kresse, G. & Furthmüller, J. Efficiency of ab-initio total energy calculations for metals and semiconductors using a plane-wave basis set. *Comput. Mater. Sci.* **6**, 15–50 (1996).
84. Blöchl, P. E. Projector augmented-wave method. *Phys. Rev. B* **50**, 17953–17979 (1994).
85. Kresse, G. D. J. From ultrasoft pseudopotentials to the projector augmented-wave method. *Phys. Rev. Lett.* **59**, 1758–1775 (1999).
86. Perdew, J. P., Burke, K. & Ernzerhof, M. Generalized gradient approximation made simple. *Phys. Rev. Lett.* **77**, 3865–3868 (1996).
87. Henkelman, G. & Jónsson, H. Improved tangent estimate in the nudged elastic band method for finding minimum energy paths and saddle points. *J. Chem. Phys.* **113**, 9978–9985 (2000).
88. Henkelman, G., Uberuaga, B. P. & Jónsson, H. A climbing image nudged elastic band method for finding saddle points and minimum energy paths. *J. Chem. Phys.* **113**, 9901–9904 (2000).

Acknowledgements

This work was supported by the National Key R&D Program of China (2023YFB3809101). Q.L. acknowledges the support of the National Natural Science Foundation of China (U23A20128) and the Chongqing Science and Technology Commission of China (CSTC2024YCJH-BGZXM0041). We appreciate the Analytical and Testing Center of Chongqing University for their technical support. We are grateful to Yijian Chen for his assistance on DFT calculations.

Author contributions

Y.L. proposed the idea behind the research. Y.L. and Qi.L. co-supervised the project. T.S. performed the synthesis, characterization, property measurements and DFT calculations. X.S. and Qu.L. conducted Vickers hardness tests. T.S. and Y.Z. analyzed SEM and TEM data. Z.T. and J.L. conducted a long-cycle stability test. T.S., J.L., and Y.L. co-wrote the paper. All authors discussed the results and commented on the manuscript.

Competing interests

The authors declare no competing interests.

Additional information

Supplementary information The online version contains supplementary material available at <https://doi.org/10.1038/s41467-026-68390-8>.

Correspondence and requests for materials should be addressed to Yangfan Lu.

Peer review information *Nature Communications* thanks Wenjie Song and the other anonymous reviewer(s) for their contribution to the peer review of this work. A peer review file is available.

Reprints and permissions information is available at <http://www.nature.com/reprints>

Publisher's note Springer Nature remains neutral with regard to jurisdictional claims in published maps and institutional affiliations.

Open Access This article is licensed under a Creative Commons Attribution-NonCommercial-NoDerivatives 4.0 International License, which permits any non-commercial use, sharing, distribution and reproduction in any medium or format, as long as you give appropriate credit to the original author(s) and the source, provide a link to the Creative Commons licence, and indicate if you modified the licensed material. You do not have permission under this licence to share adapted material derived from this article or parts of it. The images or other third party material in this article are included in the article's Creative Commons licence, unless indicated otherwise in a credit line to the material. If material is not included in the article's Creative Commons licence and your intended use is not permitted by statutory regulation or exceeds the permitted use, you will need to obtain permission directly from the copyright holder. To view a copy of this licence, visit <http://creativecommons.org/licenses/by-nc-nd/4.0/>.

© The Author(s) 2026